ANNUAL REVIEWS

Annual Review of Physical Chemistry

Modeling Spin-Crossover Dynamics

Saikat Mukherjee,[1] Dmitry A. Fedorov,[2] and Sergey A. Varganov[3]

[1]Institut de Chimie Radicalaire, CNRS 7273, Aix-Marseille University, 13013 Marseille, France; email: saikat.mukherjee@univ-amu.fr

[2]Oak Ridge Associated Universities, Oak Ridge, Tennessee 37830, USA; email: dfedorov@nevada.unr.edu

[3]Department of Chemistry, University of Nevada, Reno, Nevada 89557-0216, USA; email: svarganov@unr.edu

Annu. Rev. Phys. Chem. 2021. 72:515–40

First published as a Review in Advance on February 9, 2021

The *Annual Review of Physical Chemistry* is online at physchem.annualreviews.org

https://doi.org/10.1146/annurev-physchem-101419-012625

Keywords

nonadiabatic molecular dynamics, spin-orbit coupling, intersystem crossings, spin-forbidden reactions

Abstract

In this article, we review nonadiabatic molecular dynamics (NAMD) methods for modeling spin-crossover transitions. First, we discuss different representations of electronic states employed in the grid-based and direct NAMD simulations. The nature of interstate couplings in different representations is highlighted, with the main focus on nonadiabatic and spin-orbit couplings. Second, we describe three NAMD methods that have been used to simulate spin-crossover dynamics, including trajectory surface hopping, ab initio multiple spawning, and multiconfiguration time-dependent Hartree. Some aspects of employing different electronic structure methods to obtain information about potential energy surfaces and interstate couplings for NAMD simulations are also discussed. Third, representative applications of NAMD to spin crossovers in molecular systems of different sizes and complexities are highlighted. Finally, we pose several fundamental questions related to spin-dependent processes. These questions should be possible to address with future methodological developments in NAMD.

1. INTRODUCTION

Nonradiative transitions between electronic states with different spin multiplicities play important roles in many areas of molecular science, as is evident from the different names used for these processes, including spin crossovers (1, 2), intersystem crossings (3), spin-forbidden reactions (4), and two- or multistate reactivity (5). These transitions, which we call spin crossovers here for consistency, can be initiated by various stimuli, such as light, temperature, pressure, and an external magnetic field. The concepts of spin crossover and internal conversion (IC), transitions between electronic states with the same spin, are rooted in two approximations central to quantum chemistry. The Born-Oppenheimer approximation (BOA) separates electronic and nuclear motions, while the spin-free Hamiltonian in the nonrelativistic Schrödinger equation decouples electronic motion from electron spin. These approximations lead to nuclei propagating adiabatically on a single electronic state with a well-defined spin. Nonadiabatic processes that are characterized by the energy transfer between the nuclear, electronic, and spin degrees of freedom (DOFs) are forbidden. However, if an energy gap between electronic states becomes small enough to be comparable to the nuclear kinetic energy or the relativistic spin-dependent energy, these approximations break down and transitions between different electronic states become allowed. The probability of transitions between electronic states with the same spin depends on the nonadiabatic coupling (NAC) defined in Section 2. The NAC between electronic states with different spins vanishes due to the orthogonality of the spin eigenfunctions. Spin crossovers are mediated by spin-dependent coupling (SDC), which mixes the electronic states of different spins and can arise from spin-orbit, spin-spin, hyperfine, and external magnetic field interactions. Here, we mostly focus on the spin-orbit coupling (SOC), which usually makes the largest contribution to SDC.

Modeling spin crossovers can provide insights into photochemical reaction mechanisms, help to interpret complex vibronic spectra, calculate the rates of formally spin-forbidden reactions, and predict the lifetimes of excited electronic states. While time-independent statistical theories can be used to study spin-crossover kinetics (see the sidebar titled Nonadiabatic Statistical Theories), the nonequilibrium nature of spin crossovers often requires the use of nonadiabatic molecular dynamics (NAMD), which propagates nuclear and electronic DOFs in time (6). NAMD methods can be separated into two types. In the grid-based methods, nuclear DOFs are propagated on precomputed electronic potential energy surfaces (PESs), while in the direct dynamics methods, the electronic properties are calculated on the fly as nuclei propagate. Both types rely on electronic structure methods to obtain energies, energy gradients, and couplings for multiple electronic states at different nuclear geometries. In general, because spin crossovers and ICs can happen on a similar timescale, both types of nonadiabatic transitions have to be considered in NAMD simulations.

In NAMD, nuclear DOFs can be propagated in time on electronic states obtained in several different ways (**Figure 1**). Most electronic structure calculations solve the spin-free

NONADIABATIC STATISTICAL THEORIES

Nonadiabatic statistical theories (NASTs) assume that the rate of intramolecular energy distribution is much faster than the spin-crossover rate (7–9). These theories can account for quantum effects such as tunneling and zero-point vibrational energy (10). They are ideally suited to study the kinetics of slow spin crossovers in large complex systems for which long molecular dynamics simulations are not feasible. NASTs require electronic structure information at only a very few nuclear geometries, making them compatible with both high-level electronic structure methods (10, 11) and molecular fragmentation techniques (12).

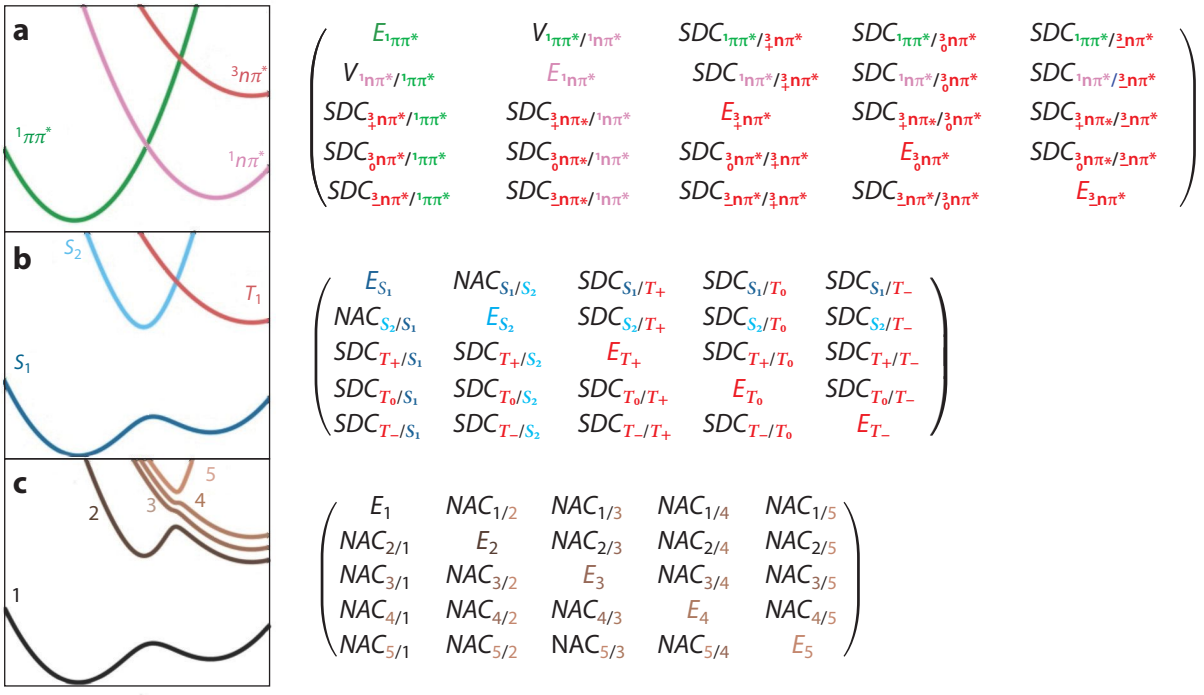

Figure 1

Electronic states in the (*a*) diabatic, (*b*) spin-diabatic, and (*c*) fully adiabatic representations with the corresponding electronic Hamiltonian matrices. The panels depict electronic states as functions of a nuclear coordinate. Abbreviations: NAC, nonadiabatic coupling; SDC, spin-dependent coupling. Part of the figure (panels with graphs) adapted with permission from Reference 14; copyright 2015 John Wiley & Sons.

time-independent Schrödinger equation within the BOA, producing a separate manifold of adiabatic electronic states for each spin multiplicity. As their name suggests, these states correspond to electrons instantaneously adjusting to nuclear motion and can have mixed character (for example, $\pi\pi^*/n\pi^*$ character). However, because the Hamiltonian has no spin-dependent terms, the states from different spin manifolds do not mix. We call this representation spin diabatic (13); it also has been called the molecular Coulomb Hamiltonian representation (14). The breakdown of the BOA introduces NAC between the spin-diabatic states with the same spin, and the addition of the spin-dependent terms into the Hamiltonian leads to SDC between the states with different spins (**Figure 1*b***). While the spin-diabatic states are relatively easy to obtain, the crossings of N_N-dimensional PESs of the same-spin states produce the $(N_N - 2)$-dimensional conical intersections (CIs) with singular NAC (avoided crossings for $N_N = 1$; N_N is the number of nuclear DOFs). These features present challenges for propagating nuclear DOFs, especially if the PESs and coupling surfaces have to be fitted for grid-based NAMD. Smooth PESs and couplings can be obtained by transformation into the diabatic representation, in which electronic states preserve their character, and the singular NAC is replaced by the smooth interstate coupling V (**Figure 1*a***). However, for polyatomic molecules, only an approximate diabatization can be achieved (15), and, at least for some NAMD methods, the diabatic representation leads to less accurate results (14, 16). Spin-diabatic states can also be transformed into the fully adiabatic representation by eliminating SDC at the expense of introducing the nonzero NAC between the resulting spin-mixed states

(**Figure 1*c***). While adiabatic PESs and NAC surfaces are not suitable for fitting, the NAC localized at CIs and the ability to describe each component of spin multiplets separately (see states 3, 4, and 5 in **Figure 1*c***) make this representation desirable for direct dynamics (13, 14). In general, performing NAMD simulations in the fully adiabatic representation requires the implementations of the analytical energy gradient and NAC for spin-mixed states, which is still a challenge; however, an approximate on-the-fly adiabatization has been implemented (14).

In Section 2, we review the NAMD and some aspects of electronic structure methods for modeling spin-crossover dynamics. While many different flavors of NAMD have been developed to describe IC dynamics at CIs, and some of them potentially could be extended to model spin-dependent processes, we limit our discussion to the methods that have been applied to spin crossovers. In Section 3, we describe a few representative applications of these methods to molecular systems of different complexity. We conclude by posing several fundamental questions related to spin-dependent processes. These questions should be possible to address with future methodological developments in NAMD.

2. METHODS FOR MODELING SPIN-CROSSOVER DYNAMICS

In this section, we describe three types of NAMD used to model spin-crossover dynamics. The stochastic trajectory surface hopping (TSH) method solves the time-dependent Schrödinger equation (TDSE) for electrons while propagating classical nuclei. In the multiple spawning method, the nuclear wave function is expanded in the adaptive basis set of frozen Gaussians propagating in time. In the multiconfiguration time-dependent Hartree (MCTDH) method, the nuclear wave function is represented as a superposition of the multidimensional products of basis functions, in which both the superposition coefficients and the basis functions are time dependent. In principle, all three types of NAMD can be performed on the precomputed (usually diabatic) PESs or as direct dynamics (usually using the spin-diabatic or fully adiabatic representation). However, the strength of the TSH and multiple spawning methods is in direct dynamics, while MCTDH was originally developed as a grid-based method. Finally, because any NAMD simulation requires accurate electronic energies, gradients, and interstate couplings, we discuss several aspects of the electronic structure methods used to model spin-crossover dynamics.

2.1. Trajectory Surface Hopping

In the TSH method, the nuclear wave packet is represented as a swarm of independent trajectories obeying the classical Newtonian equations of motion (EOMs). The force acting on the nuclei is equal to the negative energy gradient of the corresponding electronic state (17–19). At each time step, a stochastic process determines whether the system propagates on the current electronic state or hops to another state, leading to population transfer between the states. The classical propagation and purely local nature of nuclei make the TSH method easy to implement and therefore widespread (20–22). Although TSH was originally formulated to describe ICs, it has been extended to model spin crossovers (13, 23–26). González and coworkers (14, 23) introduced the surface hopping including arbitrary couplings (SHARC) method with on-the-fly adiabatization of spin-diabatic states. Persico and coworkers (13, 27) included SOC in the TSH method to study spin crossovers in both spin-diabatic and fully adiabatic representations.

We define the full electron-nuclear Hamiltonian $\hat{H}$ as the sum of the nuclear kinetic energy $\hat{T}_{\mathrm{N}}$, the spin-free electronic Hamiltonian $\hat{H}_0$, and the SOC operator $\hat{H}_{\mathrm{SOC}}$:

$$\hat{H}(\mathbf{r},\ \mathbf{R},\ \mathbf{s}) = \hat{T}_{\mathrm{N}}(\mathbf{R}) + \hat{H}_0(\mathbf{r},\ \mathbf{R}) + \hat{H}_{\mathrm{SOC}}(\mathbf{r},\mathbf{R},\mathbf{s}), \qquad 1.$$

where **r**, **R**, and **s** are vectors of the electronic, nuclear, and spin DOFs, respectively. The nuclear–nuclear repulsion is included in $\hat{H}_0$. The time-dependent electronic wave function is expanded in the basis set of N_e time-independent electronic states ϕ_I that depend parametrically on nuclear positions:

$$\psi(\mathbf{r},\mathbf{s},t;\mathbf{R}) = \sum_{I}^{N_e} c_I(t)\phi_I(\mathbf{r},\mathbf{s};\mathbf{R}). \quad 2.$$

Inserting this wave function into the electronic TDSE with the Hamiltonian $\hat{H}_0 + \hat{H}_{SOC}$ yields the EOMs for the coefficients (we use the atomic units with $\hbar = 1$):

$$i\dot{c}_I = \sum_{J}^{N_e} \left(H_{IJ}^0 + H_{IJ}^{SOC} - i\sigma_{IJ}^{NAC}\right) c_J, \quad 3.$$

where a dot above a variable indicates a time derivative and H_{IJ}^0 and H_{IJ}^{SOC} are the matrix elements of the spin-free and SOC Hamiltonians, respectively. The NAC is defined as $\sigma_{IJ}^{NAC} = \langle\phi_I|\frac{\partial}{\partial t}\phi_J\rangle = \mathbf{v}\cdot\mathbf{d}_{IJ}$, where **v** is the nuclear velocity vector and $\mathbf{d}_{IJ} = \langle\phi_I|\nabla_{\boldsymbol{R}}|\phi_J\rangle$ is the NAC vector. In the spin-diabatic representation, ϕ_I are the eigenfunctions of $\hat{H}_0$, and $H_{IJ}^0 = E_I\delta_{IJ}$, where E_I are the electronic state energies. If states I and J have different spin quantum numbers S_I and S_J, σ_{IJ}^{NAC} vanishes due to the orthogonality of the spin eigenfunctions. If I and J are both singlet states or $|S_I - S_J| > 1$, then H_{IJ}^{SOC} vanishes. A detailed discussion of the SOC selection rules can be found in References 28 and 29. In contrast to NAC, which is mostly localized around CIs, SOC depends only weakly on molecular geometry and can lead to interstate transitions far away from the crossing seam of two PESs (26). In the diabatic representation, the off-diagonal elements of H_{IJ}^0 are interstate couplings, while σ_{IJ}^{NAC} should vanish (in quasi-diabatic representations, usually some residual NAC is still present), and the SOC selection rules are the same as those in the spin-diabatic representation. Finally, in the fully adiabatic representation, the spin-mixed states ϕ_I are the eigenfunctions of $\hat{H}_0 + \hat{H}_{SOC}$ and are coupled by nonzero NAC. The results of TSH simulations are averaged over a swarm of trajectories with initial conditions sampled from some position-momentum distribution (30, 31).

Among various strategies to compute the probability of transitions between electronic states, Tully's fewest switches surface hopping (FSSH) algorithm (32) is the most common. In the generalized FSSH algorithm, the hopping probability from state I to state J in the time interval Δt is

$$P_{I\to J}^{FSSH} = \max\left(0,\ \frac{2\Delta t}{\rho_{II}}\left\{Im\left[\rho_{IJ}(H_{IJ}^0 + H_{IJ}^{SOC})\right] - Re\left[\rho_{IJ}\sigma_{IJ}^{NAC}\right]\right\}\right), \quad 4.$$

where $\rho_{IJ} = c_I c_J^*$ are the elements of the electronic density matrix. For a successful hop, two conditions must be fulfilled simultaneously. First, for a random number r selected from the interval [0,1], the following must be true:

$$\sum_{K=1}^{J-1} P_{I\to K}^{FSSH} < r \le \sum_{K=1}^{J} P_{I\to K}^{FSSH}. \quad 5.$$

Second, because the electronic energy changes as a result of the hop, to conserve the total energy, the nuclear kinetic energy must be adjusted by rescaling the nuclear velocity vector. If velocity rescaling along the NAC vector cannot compensate for the electronic energy change, the hop is rejected, and the velocity component along the NAC vector is reversed (33). This is known as a frustrated hop. Truhlar and coworkers (34) introduced the fewest switches with time uncertainty method, in which a classically frustrated hop can occur if an allowed hopping geometry can be reached within the Heisenberg interval of time uncertainty. The TSH dynamics can also be

SPIN DECOHERENCE IN MOLECULAR MAGNETS AND QUBITS

Electron spin and orbital angular momentum are responsible for the magnetic properties of the atomic and molecular systems that have been proposed for high-density memory and quantum information applications (49, 50, 51). In molecular magnets, spin relaxation (population transfer between spin states) is responsible for the loss of magnetization, while spin decoherence is related to the loss of quantum information in spin qubits. The ability to predict the spin relaxation (T_1) and decoherence (T_2) times is critical for the development of practical spin-based molecular magnets and qubits with long lifetimes. Depending on the system and operating temperature, spin-vibronic and hyperfine interactions can be responsible for electron spin relaxation and decoherence (52–54).

performed using the Landau-Zener formula (35, 36) or the more sophisticated Zhu-Nakamura formula (37, 38) to calculate the hopping probability at the crossings between electronic states. Standard FSSH formulation suffers from an overcoherence problem (39, 40), which implies that the off-diagonal density matrix elements ρ_{IJ} do not necessarily decay during the dynamics (see the sidebar titled Spin Decoherence in Molecular Magnets and Qubits). Several decoherence correction schemes have been proposed (39, 41–44) to correct for this behavior. Although the FSSH algorithm is often criticized as being an ad hoc theory, there have been attempts to show that decoherence-corrected surface hopping can be obtained from the mixed quantum-classical Liouville equation (45–48).

2.2. Multiple Spawning

The multiple spawning method belongs to a family of techniques in which the nuclear wave function is represented as a linear combination of the Gaussian basis functions that are local in nuclear configuration space (55). In the full multiple spawning (FMS) method (56, 57), these trajectory basis functions (TBFs) propagate in time on multiple electronic states. If TBFs are properly distributed in configuration space, FMS approaches the exact solution of the TDSE. However, for systems with more than a few DOFs, propagating a large number of TBFs is too computationally expensive. To minimize the basis set size without a significant loss of accuracy, FMS uses the adaptive basis set that is expanded by spawning new TBFs in the regions of strong coupling between electronic states (**Figure 2**). In principle, FMS can be employed as a grid-based method requiring the global knowledge of PESs and couplings. However, the strength of localized TBFs is fully utilized in the direct dynamics ab initio multiple spawning (AIMS) method (57–59), which uses the saddle-point approximation (SPA) and the independent first-generation approximation (IFGA) (60).

The FMS/AIMS formalism is based on the expansion of the total wave function in the basis set of the electronic wave functions ϕ_I:

$$\psi(\mathbf{r}, \mathbf{s}, \mathbf{R}, t) = \sum_{I}^{N_e} \chi^I(\mathbf{R}; t)\phi_I(\mathbf{r}, \mathbf{s}; \mathbf{R}). \quad 6.$$

The nuclear wave functions χ^I are superpositions of the multidimensional Gaussian TBFs χ_i^I,

$$\chi^I(\mathbf{R}, t) = \sum_{i}^{N_{TBF}} C_i^I(t)\ \chi_i^I(\mathbf{R}; \bar{\mathbf{R}}_i^I(t), \bar{\mathbf{P}}_i^I(t), \bar{\gamma}_i^I(t), \boldsymbol{\alpha}), \quad 7.$$

where $C_i^I(t)$ are complex amplitudes and N_{TBF} is the total number of TBFs. Each TBF follows a classical trajectory with the position and momentum centers $\bar{\mathbf{R}}_i^I(t)$ and $\bar{\mathbf{P}}_i^I(t)$ propagating on the electronic state I according to the classical Hamilton EOMs, while the phase $\bar{\gamma}_i^I(t)$ propagates

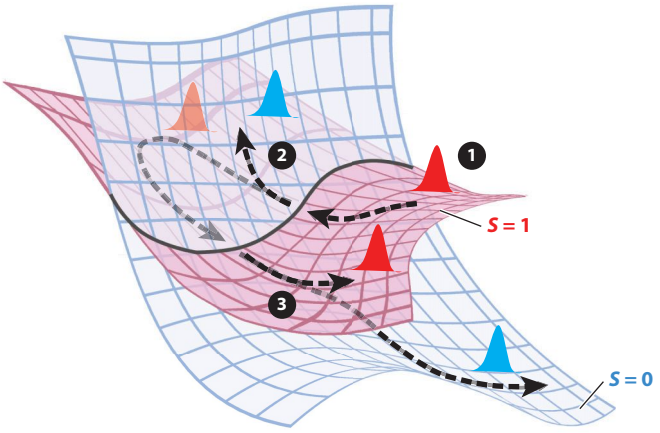

Figure 2

Illustration of trajectory basis functions (TBFs) propagating along the dashed arrows and spawning on spin-diabatic potential energy surfaces. ❶ Simulations start with a TBF (*red Gaussian*) on the triplet state ($S = 1$). ❷ Once this TBF reaches the seam region with strong interstate coupling, it spawns a new TBF (*blue Gaussian*) to the singlet state ($S = 0$). ❸ After returning to the seam region, the red TBF spawns a second blue TBF to the singlet state. The amount of population transferred between TBFs depends on the quantum amplitudes obtained by solving the time-dependent Schrödinger equation. Figure adapted with permission from Reference 62; copyright 2016 American Chemical Society.

semiclassically. The time-independent Gaussian widths collected in the vector $\boldsymbol{\alpha}$ are parametrized for each type of nucleus. The following EOMs for amplitudes is obtained by inserting Equations 6 and 7 into the TDSE:

$$i\mathbf{S}_{II}\dot{\mathbf{C}}_I = \sum_J^{N_c}(\mathbf{H}_{IJ} - i\dot{\mathbf{S}}_{II})\mathbf{C}_J. \quad 8.$$

Equation 8 is written in matrix form, with the elements of the overlap and Hamiltonian matrices defined as

$$(S_{II})_{ij} = \left\langle \chi_i^I | \chi_j^I \right\rangle, \quad 9.$$

$$(\dot{S}_{II})_{ij} = \left\langle \chi_i^I \left| \frac{\partial}{\partial t} \chi_j^I \right. \right\rangle, \text{ and} \quad 10.$$

$$(H_{IJ})_{ij} = \left\langle \chi_i^I \phi_I | \hat{T}_N + \hat{H}_0 + \hat{H}_{SOC} | \phi_J \chi_j^J \right\rangle. \quad 11.$$

The overlap matrix elements and their time derivatives arise due to the nonorthogonality of TBFs propagating on the same electronic state. The diagonal Hamiltonian matrix elements are electronic state energies, and the off-diagonal elements are interstate couplings. In contrast to the independent trajectories in the TSH method, the TBFs in FMS/AIMS are coupled, which prevents overcoherence (61). The original AIMS method has been developed to study ICs at CIs with NAC arising from the kinetic energy matrix elements in Equation 11. To model spin crossovers between spin-diabatic states, AIMS was generalized by adding SOC to the Hamiltonian (62–64).

The matrix elements in Equation 11 are obtained by integration over all electronic, nuclear, and spin DOFs, which requires knowledge of the entire potential energy and coupling surfaces. The SPA makes the direct AIMS dynamics possible by using the Taylor expansion to approximate

these matrix elements. In the zeroth-order SPA, the matrix elements between two TBFs centered at $\bar{\mathbf{R}}_i^I$ and $\bar{\mathbf{R}}_j^J$ are calculated at the position of their centroid $\bar{\mathbf{R}}_C$, which removes the problem of nonlocality (56, 65). For example, the SOC matrix elements are approximated as

$$\langle \chi_i^I \phi_I | \hat{H}_{\mathrm{SOC}} | \phi_J \chi_j^J \rangle \approx \langle \phi_I | \hat{H}_{\mathrm{SOC}}(\bar{\mathbf{R}}_C) | \phi_J \rangle \langle \chi_i^I | \chi_j^J \rangle. \quad 12.$$

For SOC, the SPA works very well because the magnitude of coupling does not change drastically around the state crossing.

The key feature of AIMS is an adaptive basis set that is expanded by spawning new TBFs in the regions of strong coupling between electronic states. For a TBF propagating on state I, spawning to state J with different spin is triggered if a preset threshold becomes smaller than the effective coupling parameter

$$\Lambda_{\mathrm{eff}} = \frac{\langle \phi_I | \hat{H}_{\mathrm{SOC}}(\bar{\mathbf{R}}_C) | \phi_J \rangle \langle \chi_i^I | \chi_j^J \rangle}{E_I - E_J}. \quad 13.$$

The denominator, defined as the energy gap between two states, is introduced to avoid excessive spawning far from the state crossing regions. A new TBF is created with zero amplitude and therefore zero population. This is an important distinction from the stochastic methods such as TSH, in which the mere fact of a hop means that the population has been transferred between electronic states. In AIMS, the population is transferred by solving the TDSE, accounting for quantum effects in a natural way. Although the choice of the coupling parameter ensures that spawning occurs only where a significant amount of population can be transferred, the event of spawning itself does not automatically translate into population transfer. Therefore, spawning is just an efficient and physically motivated way of reducing the basis set size. During a spawning event, classical energy conservation can be maintained by rescaling both the momentum and the position of the new TBF. The finite size of TBFs allows for significant adjustments to their momenta and positions, potentially reducing the number of frustrated spawning events compared to the number of frustrated hops in the TSH method. A detailed description of the spawning algorithm can be found in References 57, 58, and 66.

The IFGA reduces the cost of AIMS simulations by treating the initial TBFs independently. Every initial TBF stays coupled to all of the TBFs that it spawned. In contrast, in FMS every TBF is coupled to every other TBF, even to TBFs spawned by other initial basis functions, resulting in the quadratic growth of the number of matrix elements to be calculated. While rigorous, the FMS approach is inefficient because initial TBFs often move quickly away from each other, and their overlaps become negligible. Similar to TSH, the results of AIMS dynamics are averaged over multiple simulations, each starting from a single initial TBF, with positions and momenta sampled from some distribution (57, 67). Even if IFGA is applied and multiple AIMS simulations are run independently, the number of spawned basis functions in individual AIMS simulations can become too large, drastically increasing simulation time or even rendering it intractable. In such cases, a careful tuning of the spawning threshold parameter is required. In addition, this problem can be alleviated by using the recently introduced stochastic-selection AIMS (SSAIMS) method, which essentially separates groups of TBFs into independent simulations if these groups stay uncoupled during dynamics (68). Such a situation is very common in high-dimensional problems.

2.3. Multiconfiguration Time-Dependent Hartree Method

The TDSE can be solved by expanding the nuclear wave function into a time-independent orthogonal basis set, such as the eigenfunctions of a harmonic oscillator, with time-dependent coefficients. While such a grid-based approach rigorously describes the motion of a nuclear wave

packet, it scales exponentially with the number of nuclear DOFs and, therefore, is applicable only to small systems. In MCTDH (69–71), the computational cost is lowered significantly by representing a nuclear wave function as a linear combination of f-dimensional products of the single particle functions (SPFs) φ:

$$\Psi(Q_1, \ldots, Q_f, t) = \sum_{i_1=1}^{n_1} \cdots \sum_{i_f=1}^{n_f} A_{i_1 \ldots i_f}(t) \prod_{k=1}^{f} \varphi_{i_k}^{(k)}(Q_k, t), \quad 14.$$

where $Q_1, \ldots, Q_f$ are the nuclear coordinates, f is the number of nuclear DOFs, n_k is the number of SPFs for the k^{th} DOFs, and $A_{i_1 \ldots i_f}$ are the time-dependent expansion coefficients. Each SPF is expressed as a linear combination of N_k time-independent primitive basis functions χ with time-dependent coefficients:

$$\varphi_{i_k}^{(k)}(Q_k, t) = \sum_{j_k=1}^{N_k} c_{j_k}^{(k)}(t) \chi_{j_k}^{(k)}(Q_k). \quad 15.$$

Therefore, the MCTDH ansatz employs the standard wave-packet expansion but with time-dependent SPFs. This reduces the number of basis functions required for a converged calculation by providing the variationally determined basis for the optimal description of the evolving wave packet.

Two constraints are invoked in the formal MCTDH derivation: initially orthonormal SPFs remain orthonormal at all times, and the constraint operator ensuring the uniqueness of the nuclear wave function is Hermitian (71). The wave function defined by Equations 14 and 15 is inserted into the Dirac-Frenkel variational principle to obtain the EOMs for the time-dependent expansion coefficients and SPFs:

$$i\dot{A}_I = \sum_L \langle \Phi_I | \hat{H} | \Phi_L \rangle A_L \quad \text{and} \quad 16.$$

$$i\dot{\boldsymbol{\varphi}}^{(k)} = \left\{ h^{(k)} \mathbf{1}_{n_k} + \left[1 - P^{(k)}\right] \left[\boldsymbol{\rho}^{(k)^{-1}}\right] \langle \mathbf{H}_R \rangle^{(k)} \right\} \boldsymbol{\varphi}^{(k)}. \quad 17.$$

In Equation 16, composite indices and the configuration function Φ_I are defined as $A_I = A_{i_1 \ldots i_f}$ and $\Phi_I = \prod_{k=1}^{f} \varphi_{i_k}^{(k)}$. In Equation 17, $\boldsymbol{\varphi}^{(k)} = [\varphi_1^{(k)}, \ldots, \varphi_{n_k}^{(k)}]^T$ is the vector of SPFs, and $\mathbf{1}_{n_k}$ is the n_k-dimensional identity matrix. The Hamiltonian $\hat{H}$ is split into the separable terms $\hat{h}^{(k)}$, acting only on a single DOF, and $\hat{H}_R$, including all correlations between DOFs. $\langle \mathbf{H}_R \rangle^{(k)}$ and $\boldsymbol{\rho}^{(k)}$ are the mean-field and density matrices, respectively. The projector operator $P^{(k)}$ ensures that the SPF time derivative is orthogonal to the space spanned by SPFs. The eigenfunctions of the density matrix are called natural orbitals, and the eigenvalues correspond to populations of these orbitals. As the space spanned by the natural orbitals is equivalent to that of the original SPFs, the natural orbital populations provide a measure for the quality of the MCTDH wave function. If the population of the highest natural orbital is negligibly low, this orbital (SPF) is redundant, and hence, the MCTDH wave function is of good quality. The time-dependent Hartree method is a limiting case of MCTDH, with all $n_k = 1$. The standard wave-packet expansion into a basis set of primitive functions corresponds to $n_k = N_k$. When SPFs do not form the complete basis set, the variational method ensures that the available SPFs provide the best possible basis set to describe the wave function at each time step. The EOMs (Equations 16 and 17) are coupled nonlinear differential equations that can be solved by a predictor-corrector integration scheme. However, a suitable integration scheme, called constant mean-field integration, has been designed to solve these EOMs accurately and efficiently (71, 72).

To describe nonadiabatic transitions, an extra electronic DOF with the number of SPFs equal to the number of electronic states is added. If only one set of SPFs is used to describe all electronic states, this is called a single-set formulation. If the PESs are very different from each other, a multi-set formulation with different SPF sets for each electronic state is preferable (72). A vibrational mode combination technique is introduced to further reduce the computational cost. The idea is to combine the physical coordinates into particles or logical coordinates and, thereby, shorten the size of the expansion coefficient vector. A good practice is to combine strongly correlated modes in one particle and keep all the particle grids similar in size. Alternatively, the DOFs with similar vibrational frequencies can be combined. It is advisable not to combine too many modes and not to construct particles of too large a size. Mode combination is the foundation for multilayer (ML) MCTDH (73), which was originally developed by Wang & Thoss (74) and later reformulated by Manthe (75) for an arbitrary number of layers. ML-MCTDH is very computationally efficient and can handle more than 1,000 nuclear DOFs (76), but strict convergence can be difficult to achieve.

Another important MCTDH development is the variational multiconfigurational Gaussian wave-packet (vMCG) method (77–79). However, to the best of our knowledge, it has not yet been applied to spin crossovers. The idea was inspired by the G-MCTDH method (80, 81), in which some of the SPFs are replaced by Gaussian functions. Replacing all SPFs with multidimensional frozen Gaussians, as is done in vMCG, leads to the same wave function as in the FMS method. However, the Dirac-Frenkel variational principle used in vMCG yields EOMs for the expansion coefficients and Gaussian parameters that are different from the ones in FMS. Similar to FMS/AIMS, the direct dynamics version of vMCG has been also implemented (79).

Because the grid-based MCTDH works with nonlocal PESs and couplings, the singular NAC must be removed by transforming the adiabatic or spin-diabatic electronic states to the diabatic representation (82–84). Vibronic coupling models are often used to construct the diabatic Hamiltonians (3, 85). For the model with N_e electronic states, the N_e-dimensional Hamiltonian matrix $\mathbf{H}^{\text{vib}}$ is expanded around some, usually the Frank-Condon (FC), geometry $\mathbf{Q}_0$:

$$\mathbf{H}^{\text{vib}} = (T_N + V_0)\mathbf{1} + \mathbf{W}^{(0)} + \mathbf{W}^{(1)} + \mathbf{W}^{(2)} + \ldots, \qquad 18.$$

where V_0 is the ground-state potential and $\mathbf{W}^{(0)}$ is the diagonal matrix of the vertical excitation energies. Truncating the series at $\mathbf{W}^{(1)}$ and $\mathbf{W}^{(2)}$ produces the linear vibronic coupling (LVC) and quadratic vibronic coupling (QVC) models, respectively. The LVC parameters, the diagonal forces κ, and the off-diagonal interstate couplings λ in $\mathbf{W}^{(1)}$ for each normal mode Q_i are

$$\kappa_i^I = \left.\frac{\partial V_I}{\partial Q_i}\right|_{\mathbf{Q}_0} \quad \text{and} \quad \lambda_i^{I,J} = \left(\frac{1}{8}\left.\frac{\partial^2 |V_I - V_J|^2}{\partial Q_i^2}\right|_{\mathbf{Q}_0}\right)^{1/2}, \qquad 19.$$

where V_I is the adiabatic energy of the electronic state I. The spin-vibronic Hamiltonian can be obtained as a sum of the spin-free vibronic Hamiltonian $\mathbf{H}^{\text{vib}}$ and the spin-orbit Hamiltonian $\mathbf{H}^{\text{SOC}}$ (86–90). However, the spin-vibronic Hamiltonian also can be constructed directly from the fully adiabatic spin-mixed states (91–95).

2.4. Electronic Structure Methods

Here, we discuss some practical aspects of employing different electronic structure methods to model spin-crossover dynamics. For comprehensive reviews of electronic structure methods used in NAMD, the reader is referred to References 22, 59, 61, and 96. The success of NAMD simulations depends on the accuracy of the electronic structure methods used to obtain the energies, energy gradients, and couplings for multiple electronic states at different molecular geometries, as

has been demonstrated in the recent TSH study of spin-crossover dynamics in thioformaldehyde (97). However, because the number of electronic structure calculations limits the timescale of direct NAMD simulations and the number of nuclear DOFs in grid-based dynamics, the electronic structure methods must be computationally efficient. For example, a 2-ps direct TSH simulation with the average 0.2-fs time step (often a variable time step is used) and a small sampling of over 100 trajectories requires 10^6 electronic structure calculations. Assuming the trajectories can be run in parallel, to complete them within one week requires calculating energies, gradients, and couplings for multiple electronic states approximately every minute. A similar AIMS simulation, which has to calculate matrix elements between TBFs, requires even more electronic structure calculations. For grid-based NAMD, the same 10^6 electronic structure calculations are required to build the global PESs and coupling surfaces for a system with three nuclear DOFs, assuming the calculations generate a dense 3D grid with 100 points per each DOF. Modern surface interpolation techniques have aimed to overcome the so-called curse of dimensionality by using sparse grids and focusing on the relevant parts of PESs to push the number of DOFs to 24–39 (8–13 atoms) for roughly the same number of electronic structure calculations (98–100). Constructing the vibronic Hamiltonian models commonly used with the MCTDH method is less computationally expensive. Assuming the same 100 electronic structure calculations per vibrational mode, the 15-mode LVC and QVC models require roughly $15 \times 100 = 1{,}500$ and $15^2 \times 100/2 = 11{,}250$ calculations, respectively. However, these models typically describe only small parts of PESs in the vicinity of the FC geometry. The electronic structure methods used in the direct NAMD must also be very reliable. The failure to produce smooth electronic energies, gradients, and couplings during time propagation can lead to the failure of the entire simulation.

Because of their computational efficiency, the density functional theory (DFT)- and multiconfigurational self-consistent field (MCSCF)-based methods are widely used in direct NAMD. The conventional linear-response time-dependent DFT (LR-TDDFT) method is a popular choice. However, the reliance of LR-TDDFT on a single-reference closed-shell wave function for the ground-state and singly excited configurations for excited states limits its applicability and accuracy. The situations with strongly multiconfigurational electronic states, such as diradical states in organic molecules, electronic states of transition metal complexes, and crossing seams between the ground and excited electronic states, cannot be described accurately. The excited states dominated by double excitations also cannot be modeled by conventional LR-TDDFT. Spin-flip TDDFT, which can describe the multiconfigurational and doubly excited electronic states (101), could become an important method for modeling spin-crossover dynamics.

MCSCF methods, including the complete active space self-consistent field (CASSCF) version, are well suited for direct NAMD simulation of processes in which multiple electronic configurations play an important role, assuming that relatively small active spaces can describe these processes. Efficient implementations of analytical energy gradients, NACs, and SOCs for state-averaged (SA)-CASSCF are widely available. However, neglecting the dynamic electron correlation in CASSCF can lead to incorrect energy gaps between electronic states of different character. While covalent states often have significant contributions from multiple electronic configurations and, therefore, are stabilized by the static correlation recovered by CASSCF, for ionic states dominated by a single configuration, little correlation energy is recovered. This leads to the overstabilization of covalent states with respect to ionic states, which in turn can affect the locations of state crossings and the overall outcome of NAMD simulations. Another important issue is related to the selection of the active space (102), which, ideally, should describe all possible outcomes of an NAMD simulation. However, such an active space is usually too large to be practical. Therefore, a smaller active space must be selected to describe the electronic transitions of interest and the parts of a molecule where chemical bonds are expected to break and/or form. This approach could lead

to NAMD oversampling the reaction pathways that are best described by the chosen active space at the expense of other pathways. In addition, if dynamics lead to molecular geometries that are not correctly described by the selected active space, the active space orbitals can rotate out of the active space. The results of such sudden active space changes include discontinuities in electronic energies, gradients, and couplings as well as failed CASSCF convergence, which often leads to the failure of the entire NAMD simulation.

While using post-MCSCF methods, such as multireference perturbation theory and configuration interaction, to account for dynamic electron correlation in direct NAMD is possible, it is often impractical due to the high computational cost. This has led to the development of parameterized approaches such as scaled CASSCF (103), α-CASSCF (104), and floating occupation molecular orbitals CASCI (complete active space configuration interaction) (105–107). Despite the fact that these methods were developed to model IC dynamics, they are also applicable to spin crossovers. In the future, other emerging multireference methods with analytical energy gradients, NACs, and SOCs (96) are expected to find applications in modeling spin-crossover dynamics.

For constructing the vibronic coupling Hamiltonian models commonly used in grid-based dynamics, the requirements for electronic structure methods are less stringent than they are for direct dynamics. A much smaller number of electronic structure calculations is required, and the failure of any particular calculation does not lead to the failure of the NAMD simulation. Also, implementations of analytical energy gradients and couplings, while helpful, are not required. As a result, the post-MCSCF methods, such as MS-CASPT2 (multistate complete active space second-order perturbation theory) and MR-CISD (multireference configuration interaction with single and double excitations), can be used to obtain the vibronic Hamiltonian parameters. However, these reduced requirements come at the price of restricting dynamics to the relatively small regions of PESs in which vibronic coupling models are valid.

The most common approach to calculating SOCs between spin-diabatic states is to use first-order perturbation theory with the Breit-Pauli or Douglas-Kroll-Hess spin-orbit Hamiltonians (29, 108, 109). Such calculations produce the SOC matrix elements between the individual M_S components of the spin states. The root-mean-square of these matrix elements for the two states with spins S and S' is used to define the SOC constant representing the effective coupling between two spin states (29). The SOC matrix elements have been implemented for the multireference (29, 110, 111), DFT (112–115), and single-reference (116) methods. For systems with heavy elements in which S is not a good quantum number, including complexes of third-row transition metals, lanthanides, and actinides, NAMD simulations should be carried out using the spin-adiabatic representation of electronic states, with the NAC between the spin-mixed states driving the interstate population transfer. While such spin-adiabatic simulations are starting to emerge (14, 25, 117–119), progress requires interfacing NAMD with the electronic structure methods that can calculate the analytical NAC between the spin-mixed states (120, 121).

3. APPLICATIONS

In this section, we describe several selected applications of NAMD to modeling spin crossovers in systems of different complexity. First, we focus on the SO_2 molecule, which, due to its small size and complex photophysics, has been studied with grid-based methods and several flavors of TSH dynamics. Second, we describe two test applications of the AIMS method to spin crossovers in the GeH_2 and H_2CS molecules. Finally, we highlight the capabilities of NAMD to model spin crossovers in large systems by discussing the full-dimensional direct TSH simulations of the $[Ru(bpy)_3]^{2+}$ complex and the MCTDH modeling of the active center of myoglobin protein using a reduced-dimensionality LVC model.

3.1. The SO_2 Molecule

The SO_2 molecule has been studied with different NAMD approaches, including full-dimensional grid-based quantum dynamics (86, 122) and direct TSH dynamics (123, 124). Xie et al. (122) constructed 3D PESs for the lowest singlet ($\tilde{A}^1B_1, \tilde{B}^1A_2$) and triplet ($\tilde{a}^3B_1, \tilde{b}^3A_2$) states using the multireference configuration interaction with the Davidson correction (MRCI+Q) with the full-valence active space and the aug-cc-pVTZ basis set. Only two singlet states and the lowest triplet state were included in the NAMD performed in the quasi-diabatic representation with constant SOC. The Chebyshev propagation to more than 1,200 fs was carried out in the Jacobi coordinates using the discrete variable representation (DVR) for the radial DOFs and the finite basis representation for the angular DOFs. This study showed a reasonable agreement between the calculated and experimental absorption spectra and demonstrated the effect of the lowest triplet state on the excited-state dynamics. The calculated electronic state population showed that the spin crossover between the $\tilde{B}^1A_2$ and $\tilde{a}^3B_1$ states occurs within 100 fs. Köppel and coworkers (86) also investigated the SO_2 photoexcitation dynamics with triplet states using DVR-based quantum dynamics. They obtained the PESs of the lowest six A″ states, which are symmetry-isolated from the A′ manifold, with MRCI+Q/cc-pVTZ and the full-valence active space. The triplet $M_S = \pm 1$ components were combined into the symmetric (+) and antisymmetric (–) states (**Figure 3**). Three-dimensional SOC surfaces were calculated using the Breit-Pauli Hamiltonian. After diabatization of the six-state model Hamiltonian, the NAMD simulations were initiated from the vertically excited $^1B_1$ state. After 1 ps, the populations of the $^1B_1$ and $^1A_2$ states were 24% and 41%, respectively, while 25% of the population was distributed over the two $^3B_2$ components and the

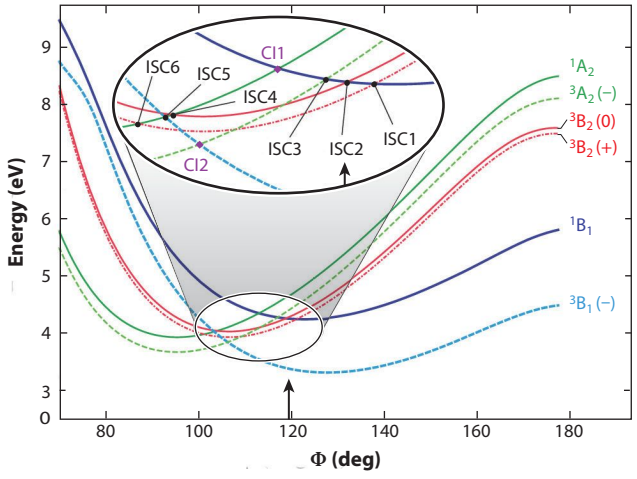

Figure 3

A graph of the lowest energy *A″* states of SO_2 showing a 1D cut through the potential energy surfaces along the bending angle. The overall dynamics is described as a three-step process with the characteristic time intervals 0–16 fs, 55–65 fs, and 150–165 fs. In the first step, the $^1B_1 \rightarrow {}^3A_2$ spin crossover occurs in the FC region around the crossing point labeled ISC3, followed by the rapid $^3A_2 \rightarrow {}^3B_1$ internal conversion through CI2. During this time, most of the singlet population is transferred to $^1A_2$ via CI1. The angle value corresponding to the FC geometry is marked by black arrows. In the second step, the $^1A_2$ population propagates into the smaller bending angle region, and the $^1A_2 \rightarrow {}^3B_1$ spin crossover takes place at ISC5. In the third step, the wave packet returns to the FC region, repeating the first-step population transfer. Abbreviations: CI, conical intersection; FC, Frank-Condon; ISC, intersystem crossing. Figure adapted with permission from Reference 86; copyright 2014 AIP Publishing.

remaining 10% decayed to $^3B_1(-)$ and $^3A_2(-)$ states. Therefore, this study confirmed the important role of the triplet states in the deactivation process of SO_2 and demonstrated the complexity of nonadiabatic dynamics, even in small molecules.

The deactivation pathways in SO_2 were also studied by González and coworkers (123) using direct TSH dynamics. They ran 111 trajectories on the four lowest singlet and three lowest triplet states calculated at the MR-CIS/ANO-RCC-VDZP level of theory with SOC calculated using the effective Fock-type spin-orbit operator. The simulations showed a rapid $^1B_1 \rightarrow {}^1A_2$ IC, followed by a significant population transfer from $^1A_2$ to $^3B_2$ with a small amount of the population going to $^3B_1$ via spin crossovers. During 700-fs dynamics, almost 50% of the total population was transferred from $^1A_2$ to $^3B_2$ with a time constant of 410 fs. Because the $^1A_2 \rightarrow {}^3A_2$ transition is El-Sayed forbidden, the population of the $^3A_2$ state at the end of the simulation was negligible. The fit of the total triplet state population produced an effective spin-crossover time constant of 540 fs. Franco de Carvalho & Tavernelli (124) performed LR-TDDFT-based TSH simulations on SO_2 in the gas and liquid phases, calculating the Landau-Zener transition probabilities at the state crossings. Two singlet (S_1 and S_2) and three triplet (T_1, T_2, and T_3) states were included in the 50-trajectory simulation. Again, a fast $S_2 \rightarrow S_1$ IC, followed by the $S_1 \rightarrow T_2$ and $S_1 \rightarrow T_3$ spin crossovers, was observed. These crossovers were followed by population transfer to T_1 via successive ICs. The liquid phase quantum mechanics/molecular mechanics simulations predicted an effective spin-crossover rate that is about twice as fast as is that in the gas phase. Recently, González and coworkers (125) parameterized an LVC model for SO_2 using only a single excited-state electronic structure calculation and a ground-state vibrational frequency calculation. The model was used to carry out a 200-trajectory TSH simulation on four singlet and three triplet diabatic states. This work demonstrated that, at least for this small system, the main timescales predicted by direct dynamics simulations can be reproduced with the LVC model dynamics while drastically reducing computational expenses.

3.2. Applications of Ab Initio Multiple Spawning to GeH_2 and H_2CS

The AIMS method has been tested on the spin crossover between the lowest excited $^3B_1$ and ground $^1A_1$ states of GeH_2 (62, 63). The spin-diabatic states were obtained using the full valence active space CASSCF and unrestricted DFT (B3LYP) methods with a 6–31G* basis set, as implemented in the General Atomic and Molecular Electronic Structure System (GAMESS) suite of programs (126). The TBFs were propagated using state-specific energies and gradients, while SOC was calculated perturbatively using the averaged over two states [SA(2)]-CASSCF orbitals and the Breit-Pauli Hamiltonian (127). In the DFT-based dynamics, SOC was also evaluated using the high-spin unrestricted DFT orbitals. The 48 initial TBFs, which started from the FC region with the initial conditions sampled from the Wigner distribution, generated about 1,200 TBFs during the 150-fs simulations. Due to the presence of a heavy atom in GeH_2, the SOC between the two states is relatively large (350 cm^{-1}), leading to a fast decay of the excited-state population. After 150 fs, around 60% of the population was transferred in both the CASSCF and DFT simulations. Surprisingly, the CASSCF- and DFT-based dynamics predicted essentially the same lifetime for the $^3B_1$ state (186 fs and 182 fs). However, this agreement is believed to be due to the fortunate cancellation of two effects: the higher spin-crossover energy barrier and the stronger SOC predicted by DFT compared to the corresponding CASSCF values.

Another implementation of the generalized AIMS method has been used to study the spin-crossover dynamics in thioformaldehyde (64). The simulations were performed at the SA(4)-CASSCF(4,3)/6–31G* level of theory and included four electronic states (S_0, S_1, T_1, and T_2). The 20 initial TBFs sampled from the Wigner distribution were started from the FC region on the

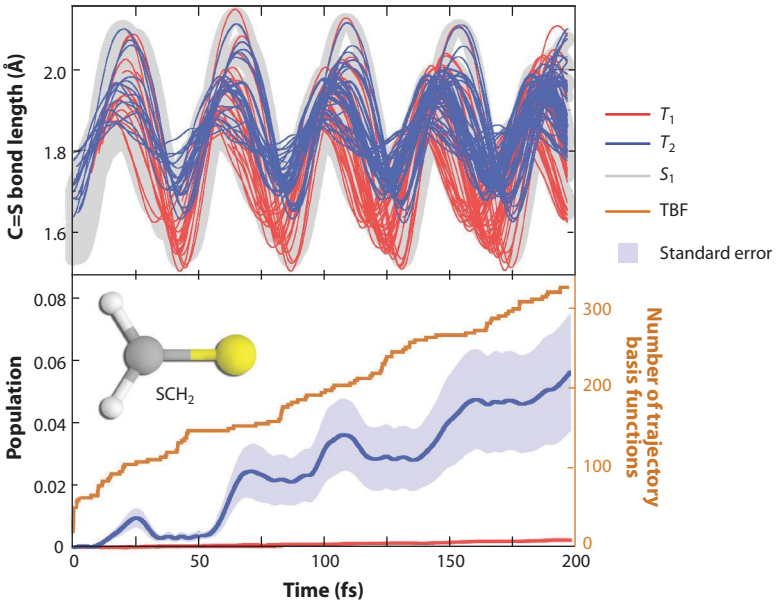

Figure 4

Generalized ab initio multiple spawning dynamics of thioformaldehyde after photoexcitation to the S_1 state. (*Top*) Graph showing C=S bond length for all trajectory basis functions (TBFs) produced during the simulation. The width of each line is proportional to the population carried by the TBF. TBFs are associated with the S_1 (*light gray*), T_1 (*red*), or T_2 (*blue*) states. (*Bottom*) Graph showing the population of the two triplet states averaged over 20 initial conditions (*light blue area* indicates the standard error). The total number of TBFs is given by the orange line. Figure adapted with permission from Reference 64; copyright 2016 AIP Publishing.

S_1 state. During the 200-fs dynamics, 326 TBFs were spawned with 306 of them on the triplet states (**Figure 4**). The population transferred to T_1 was negligible, whereas T_2 had a significant population of 8% after 200 fs. These results can be explained by El-Sayed's rule, which predicts a stronger SOC between states of different character. Therefore, the S_1 state with $n\pi^*$ character is coupled more strongly to the $\pi\pi^*$ T_2 state than to the $n\pi^*$ T_1. As the C=S bond time evolution indicates, the dynamics of TBFs on the $n\pi^*$ states S_1 and T_1 are similar, whereas the T_2 TBFs have a longer average C=S bond consistent with the $\pi\pi^*$ character of the T_2 state. While the 200-fs simulations were too short to calculate accurate spin-crossover rates, they provided valuable qualitative insight into H_2CS nonadiabatic dynamics.

The limitations of direct dynamics applied to spin crossovers arise from the generally longer timescales of these processes compared to those of ICs. In the AIMS method, the longer trajectories required for spin-crossover simulations are challenging because of the growing size of the adaptive basis set. The need to calculate the matrix elements between each TBF pair results in a superlinear growth of computational cost. Techniques to reduce the number of TBFs, such as the removal of TBFs with small contributions to the total wave function and the careful selection of spawning criteria, can significantly accelerate AIMS simulations. For high-dimensional systems, the SSAIMS method (68) can drastically reduce the computational cost by uncoupling groups of TBFs in the simulation without sacrificing accuracy. Another way to overcome the quickly growing basis set problem is to accelerate the electronic structure calculations through parallelization and the use of graphical processing units (128).

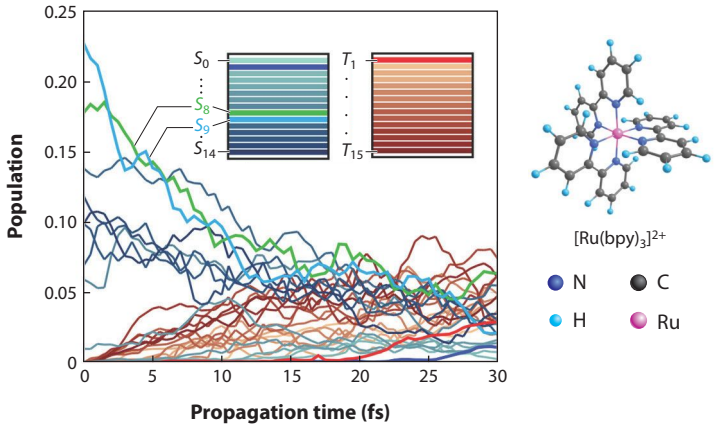

Figure 5

Trajectory surface hopping dynamics of the $[Ru(bpy)_3]^{2+}$ complex. Time-resolved normalized singlet (*blue-green*) and triplet (*red-brown*) populations over 30 fs. For the triplet states, the population is summed over different M_S components. Highlighted states are the S_1 shown in blue, the S_8 in green, the S_9 in light blue, and the T_1 in red. Figure adapted with permission from Reference 133; copyright 2017 American Chemical Society.

3.3. Large Systems

Due to its simplicity and computational efficiency, the direct TSH method is the most widely used type of NAMD to model spin crossovers in various systems (24, 25, 27, 129–135). Grid-based TSH dynamics on precomputed PESs is also used to study spin crossovers in small molecules (136–141). A recent study of the $[Ru(bpy)_3]^{2+}$ complex is an excellent example of the capability of direct TSH dynamics to model spin crossovers in large systems (133). This complex serves as a prototype for a class of compounds in which ultrafast spin crossovers occur between the singlet and triplet metal-to-ligand charge transfer (MLCT) states. The electronic energies, gradients, NACs, and SOCs were calculated with LR-TDDFT using the Perdew-Burke-Ernzerhof functional. Because the density of excited states is very high, 101 trajectories were initialized from different singlet excited states and propagated for 30 fs on a manifold of 15 singlet and 15 triplet states (**Figure 5**). Almost 65% of the total population was transferred to the triplet states corresponding to the time constant of 26 ± 3 fs, which agrees well with the experimental value of 15 ± 10 fs. Two interesting observations came out of this study. First, in contrast to Kasha's rule, the spin crossovers occur between the high-lying singlet and triplet states around the FC geometry. Second, in addition to the high density of states and strong SOC (up to 350 cm^{-1}), the vibrational motions of the N and Ru atoms play a major role in promoting the spin crossovers.

There are multiple examples of including SOC in quantum grid-based molecular dynamics (87–90, 142) (see the sidebar titled Spin Effects in Atomic–Diatomic Collisions). To overcome the curse of dimensionality in large systems, reduced-dimensionality model Hamiltonians must be constructed by choosing the most important nuclear DOFs, as was done in the recent study of the spin-crossover dynamics of CO photodissociation from the active center of the myoglobin protein (90). The geometry optimization and normal mode analysis of the singlet ground state were carried out at the B3LYP/LAN2DZ level of theory. The excited-state energies were calculated using the CASSCF(10,9)+CASPT2/ANO-RCC-VDZP level of theory, and the SOC was obtained perturbatively using the Douglas-Kroll-Hess Hamiltonian. The diabatic model Hamiltonian included 15 vibrational modes and a total of 179 singlet, triplet, and quintet electronic states. The main results of the ML-MCTDH wave-packet dynamics are presented in **Figure 6**. In the ground state,

SPIN EFFECTS IN ATOMIC–DIATOMIC COLLISIONS

The full-dimensional nonadiabatic quantum dynamics calculations on collision reactions between an atom and a diatomic molecule include the spin-orbit coupling effects (143–146). For example, considerable efforts have been devoted to constructing the spin-vibronic potential energy surfaces (PESs) for the F + H_2 reaction (147–149), in which the excited spin-orbit state $F^*(^2P_{1/2})$ plays a major role in low-energy collisions. The quantum dynamics calculations carried out on these PESs successfully reproduce the experimental collision cross sections, reaction rate constants, and branching ratios for the F + H_2/HD/D_2 reactions (146, 149–152).

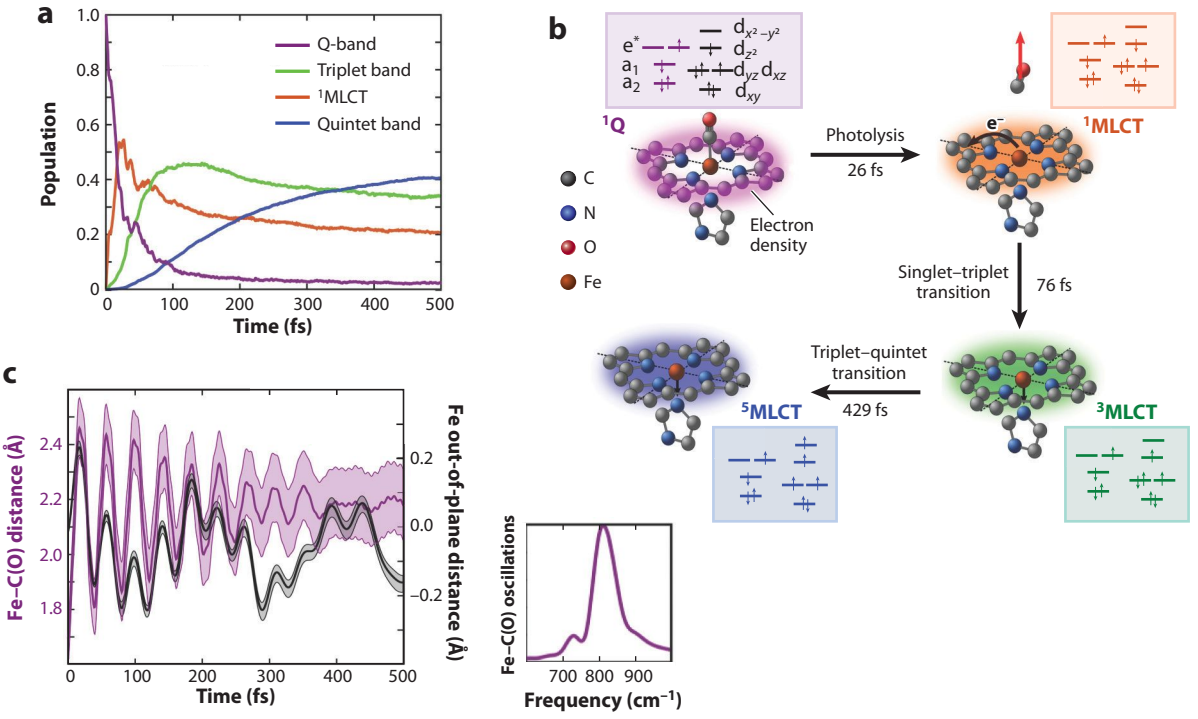

Figure 6

The quantum photodynamics of a heme–CO complex during the first 0.5 ps, with initial conditions averaged over 10 molecular dynamics snapshots. (*a*) Graph showing the evolution of diabatic populations for the states ^{1}Q (*magenta*), metal-to-ligand charge transfer (^{1}MLCT) (*orange*), triplet band (*green*), and quintet band (*blue*). The ^{1}Q population rapidly decays, giving rise to an ^{1}MLCT population that dominates by 75 fs, when the triplet population increases. The quintet population builds up more slowly and evolves into the dominant state at around 350 fs. (*b*) Schematic representation of the reaction mechanism (four molecular orbitals of porphyrin and five d orbitals of Fe are shown) and interpretation in terms of time constants. Upon initial excitation to the Q band, the MLCT state is populated in ~25 fs. In a second step, the system relaxes to the triplet state (~75 fs) and then to the lowest quintet state (~430 fs). Black arrows indicate the direction of the electron transfer and the main nuclear motions. (*c*) Graph of the evolution of the Fe–C(O) distance (*magenta*, *left* y *axis*) and the Fe out-of-plane distance (*black*, *right* y *axis*). Large-amplitude motions are observed with a period of oscillation of 40 fs. The amplitude of oscillation is initially 0.9 Å and converges toward a value of 2.2 Å. At this distance, the CO is essentially photolyzed. The standard deviation of these geometric values is shown as a shaded area. In the small graph on the right, the Fourier transform of the Fe–C(O) oscillations is shown (in reciprocal centimeters). Figure adapted with permission from Reference 90 (CC BY-SA 4.0).

Fe(II) resides in the porphyrin plane with the Fe(II)–CO distance of 1.80 Å. Upon photoexcitation to the bright singlet Q band, the complex experiences Jahn-Teller symmetry breaking and population transfer to the singlet ^{1}MLCT states within 26 fs. Because the ^{1}MLCT states are strongly spin-orbit coupled to the triplet ^{3}MLCT manifold, a rapid singlet–triplet spin crossover takes place. Finally, the population is transferred from ^{3}MLCT to the quintet ^{5}MLCT state, leading to CO dissociation and Fe moving out of the porphyrin plane into a square-pyramidal geometry. The predicted time constants for the singlet–triplet and triplet–quintet spin crossovers (76 ± 15 fs and 429 ± 70 fs) are in excellent agreement with the experimental rates.

4. CONCLUSIONS AND FUTURE DIRECTIONS

In the last decade, spin-crossover dynamics has evolved from a somewhat exotic niche within the field of nonadiabatic dynamics primarily concerned with ICs at CIs to a very active area of research. This rapid development has been driven by the realization that, despite being mediated by relativistic effects, spin crossovers can occur on a timescale similar to that of ICs, even in molecules without heavy atoms in which the relativistic effects have been traditionally neglected. Expanding the capability of NAMD to model spin crossovers has led to great interest in nonadiabatic dynamics in the transitional metal and even lanthanide complexes, in which spin-dependent processes play a central role. These new methodological developments have also raised multiple fundamental questions: How strong can the SOC be before we need to completely abandon the spin-diabatic representation of electronic states and, therefore, the concept of the spin crossover? When can the spin-dependent relativistic effects be accounted for using perturbation theory, and when must they be treated variationally at the molecular orbital level (interestingly, the perturbation approach seems to work reasonably well for lanthanide complexes)? Can higher-order effects such as spin-spin and hyperfine couplings drive spin crossovers, especially if SOC is small, as occurs between states with $\Delta S > 1$? Can an external magnetic field be used to control the spin-crossover rates in photochemistry, thermally activated spin-forbidden reactions, and molecular magnets, similar to ultracold barrierless reactions (153)? The future development of the NAMD and electronic structure methods, some of which we attempted to describe in this review, should help to answer these questions.

SUMMARY POINTS

1. Spin crossovers, transitions between electronic states with different spin multiplicities, are common and can be initiated by different stimuli, including light, temperature, pressure, and an external magnetic field.
2. While spin crossovers mediated by the relatively weak spin-orbit coupling (SOC) and higher-order couplings often occur on a slower timescale than do internal conversions (ICs), these two types of nonadiabatic processes can compete with each other.
3. The nonadiabatic molecular dynamics (NAMD) methods originally developed to simulate ICs have been extended to model spin-crossover dynamics, with the goals of predicting spin-crossover rates and gaining insights into reaction mechanisms involving electronic states with different spins.
4. Because building full-dimensional potential energy and interstate coupling surfaces is not practical for systems with more than a few nuclear degrees of freedom, the direct and

reduced-dimensionality NAMD methods are the most common approaches to modeling spin-crossover dynamics.

5. NAMD simulations require accurate and computationally efficient electronic structure methods. These methods must produce accurate energies, energy gradients, and couplings for multiple electronic states at different molecular geometries.

FUTURE ISSUES

1. At what point do relativistic effects become too strong to justify working with the spin-diabatic electronic states?
2. How can slow spin crossovers be modeled using NAMD? Perhaps some combination of short NAMD simulations and nonadiabatic statistical theories can be developed.
3. Can higher-order effects such as spin-spin and hyperfine couplings influence spin-crossover rates? This is especially important for situations in which the SOC is small.
4. Can the effect of an external magnetic field on spin-crossover rates be modeled with NAMD? This should help researchers to understand how spin-crossover dynamics can be controlled with a magnetic field.
5. Can computationally efficient multireference electronic structure methods be developed for direct NAMD? Such methods must account for dynamic electron correlation and have analytical energy gradients, nonadiabatic coupling, and SOC.

DISCLOSURE STATEMENT

The authors are not aware of any affiliations, memberships, funding, or financial holdings that might be perceived as affecting the objectivity of this review.

ACKNOWLEDGMENTS

The authors thank Todd Martínez, Basile Curchod, Edward Hohenstein, Benjamin Levine, and Dmitry G. Fedorov for fruitful discussions. This material is based on work supported by the National Science Foundation (CAREER award CHE-1654547). The authors would also like to acknowledge the donors of the American Chemical Society Petroleum Research Fund for partial support of this research (award 60481-ND6).

LITERATURE CITED

1. Halcrow MA, ed. 2013. *Spin-Crossover Materials: Properties and Applications*. Oxford, UK: John Wiley & Sons
2. Swart M, Costas M, eds. 2015. *Spin States in Biochemistry and Inorganic Chemistry*. Oxford, UK: John Wiley & Sons
3. Penfold TJ, Gindensperger E, Daniel C, Marian CM. 2018. Spin-vibronic mechanism for intersystem crossing. *Chem. Rev.* 118(15):6975–7025
4. Harvey JN. 2014. Spin-forbidden reactions: computational insight into mechanisms and kinetics. *WIREs Comput. Mol. Sci.* 4(1):1–14

5. Shaik S. 2020. Two-state reactivity: personal recounting of its conception and future prospects. *Isr. J. Chem.* 60(10–11):938–56
6. Agostini F, Curchod BFE. 2019. Different flavors of nonadiabatic molecular dynamics. *WIREs Comput. Mol. Sci.* 9(5):e1417
7. Lykhin AO, Kaliakin DS, DePolo GE, Kuzubov AA, Varganov SA. 2016. Nonadiabatic transition state theory: application to intersystem crossings in the active sites of metal-sulfur proteins. *Int. J. Quantum Chem.* 116(10):750–61
8. Jasper AW. 2015. Multidimensional effects in nonadiabatic statistical theories of spin-forbidden kinetics: a case study of $^3O + CO \rightarrow CO_2$. *J. Phys. Chem. A* 119(28):7339–51
9. Harvey JN. 2007. Understanding the kinetics of spin-forbidden chemical reactions. *Phys. Chem. Chem. Phys.* 9(3):331–43
10. Lykhin AO, Varganov SA. 2020. Intersystem crossing in tunneling regime: $T_1 \rightarrow S_0$ relaxation in thiophosgene. *Phys. Chem. Chem. Phys.* 22(10):5500–8
11. Pokhilko P, Shannon R, Glowacki D, Wang H, Krylov AI. 2019. Spin-forbidden channels in reactions of unsaturated hydrocarbons with $O(^3P)$. *J. Phys. Chem. A* 123(2):482–91
12. Kaliakin DS, Fedorov DG, Alexeev Y, Varganov SA. 2019. Locating minimum energy crossings of different spin states using the fragment molecular orbital method. *J. Chem. Theory Comput.* 15(11):6074–84
13. Granucci G, Persico M, Spighi G. 2012. Surface hopping trajectory simulations with spin-orbit and dynamical couplings. *J. Chem. Phys.* 137(22):22A501
14. Mai S, Marquetand P, González L. 2015. A general method to describe intersystem crossing dynamics in trajectory surface hopping. *Int. J. Quantum Chem.* 115(18):1215–31
15. Mead CA, Truhlar DG. 1982. Conditions for the definition of a strictly diabatic electronic basis for molecular systems. *J. Chem. Phys.* 77(12):6090–98
16. Tully JC. 1998. Mixed quantum-classical dynamics. *Faraday Discuss.* 110:407–19
17. Tully JC, Preston RK. 1971. Trajectory surface hopping approach to nonadiabatic molecular collisions: the reaction of H^+ with D_2. *J. Chem. Phys.* 55(2):562–72
18. Barbatti M. 2011. Nonadiabatic dynamics with trajectory surface hopping method. *WIREs Comput. Mol. Sci.* 1(4):620–33
19. Wang L, Akimov A, Prezhdo OV. 2016. Recent progress in surface hopping: 2011–2015. *J. Phys. Chem. Lett.* 7(11):2100–12
20. Marquetand P, Richter M, González-Vázquez J, Sola I, González L. 2011. Nonadiabatic ab initio molecular dynamics including spin-orbit coupling and laser fields. *Faraday Discuss.* 153:261–73
21. Persico M, Granucci G. 2014. An overview of nonadiabatic dynamics simulations methods, with focus on the direct approach versus the fitting of potential energy surfaces. *Theor. Chem. Acc.* 133(9):1526
22. Crespo-Otero R, Barbatti M. 2018. Recent advances and perspectives on nonadiabatic mixed quantum-classical dynamics. *Chem. Rev.* 118(15):7026–68
23. Richter M, Marquetand P, González-Vázquez J, Sola I, González L. 2011. SHARC: ab initio molecular dynamics with surface hopping in the adiabatic representation including arbitrary couplings. *J. Chem. Theory Comput.* 7(5):1253–58
24. Cui G, Thiel W. 2014. Generalized trajectory surface-hopping method for internal conversion and intersystem crossing. *J. Chem. Phys.* 141(12):124101
25. Martínez-Fernández L, Corral I, Granucci G, Persico M. 2014. Competing ultrafast intersystem crossing and internal conversion: a time resolved picture for the deactivation of 6-thioguanine. *Chem. Sci.* 5(4):1336–47
26. Zaari RR, Varganov SA. 2015. Nonadiabatic transition state theory and trajectory surface hopping dynamics: intersystem crossing between $^3B_1$ and $^1A_1$ states of SiH_2. *J. Phys. Chem. A* 119(8):1332–38
27. Favero L, Granucci G, Persico M. 2013. Dynamics of acetone photodissociation: a surface hopping study. *Phys. Chem. Chem. Phys.* 15(47):20651–61
28. Marian CM. 2001. Spin-orbit coupling in molecules. In *Reviews in Computational Chemistry*, Vol. 17, ed. KB Lipkowitz, DB Boyd, pp. 99–204. New York: John Wiley & Sons
29. Fedorov DG, Koseki S, Schmidt MW, Gordon MS. 2003. Spin-orbit coupling in molecules: chemistry beyond the adiabatic approximation. *Int. Rev. Phys. Chem.* 22(3):551–92

30. Sun L, Hase WL. 2010. Comparisons of classical and Wigner sampling of transition state energy levels for quasiclassical trajectory chemical dynamics simulations. *J. Chem. Phys.* 133(4):044313
31. Barbatti M, Sen K. 2016. Effects of different initial condition samplings on photodynamics and spectrum of pyrrole. *Int. J. Quantum Chem.* 116(10):762–71
32. Tully JC. 1990. Molecular dynamics with electronic transitions. *J. Chem. Phys.* 93(2):1061–71
33. Hammes-Schiffer S, Tully JC. 1994. Proton transfer in solution: molecular dynamics with quantum transitions. *J. Chem. Phys.* 101(6):4657–67
34. Jasper AW, Stechmann SN, Truhlar DG. 2002. Fewest-switches with time uncertainty: a modified trajectory surface-hopping algorithm with better accuracy for classically forbidden electronic transitions. *J. Chem. Phys.* 116(13):5424–31
35. Hu W, Lendvay G, Maiti B, Schatz GC. 2008. Trajectory surface hopping study of the $O(^3P)$ + ethylene reaction dynamics. *J. Phys. Chem. A* 112(10):2093–103
36. Rajak K, Maiti B. 2014. Trajectory surface hopping study of the $O(^3P) + C_2H_2$ reaction dynamics: effect of collision energy on the extent of intersystem crossing. *J. Chem. Phys.* 140(4):044314
37. Xu C, Yu L, Zhu C, Yu J, Cao Z. 2016. Intersystem crossing-branched excited-state intramolecular proton transfer for o-nitrophenol: an ab initio on-the-fly nonadiabatic molecular dynamic simulation. *Sci. Rep.* 6:26768
38. Yue L, Yu L, Xu C, Lei Y, Liu Y, Zhu C. 2017. Benchmark performance of global switching versus local switching for trajectory surface hopping molecular dynamics simulation: *cis* ↔ *trans* azobenzene photoisomerization. *Chem. Phys. Chem.* 18(10):1274–87
39. Schwartz BJ, Bittner ER, Prezhdo OV, Rossky PJ. 1996. Quantum decoherence and the isotope effect in condensed phase nonadiabatic molecular dynamics simulations. *J. Chem. Phys.* 104(15):5942–55
40. Subotnik JE, Jain A, Landry B, Petit A, Ouyang W, Bellonzi N. 2016. Understanding the surface hopping view of electronic transitions and decoherence. *Annu. Rev. Phys. Chem.* 67:387–417
41. Jasper AW, Truhlar DG. 2005. Electronic decoherence time for non-Born-Oppenheimer trajectories. *J. Chem. Phys.* 123(6):064103
42. Granucci G, Persico M, Zoccante A. 2010. Including quantum decoherence in surface hopping. *J. Chem. Phys.* 133(13):134111
43. Subotnik JE, Shenvi N. 2011. A new approach to decoherence and momentum rescaling in the surface hopping algorithm. *J. Chem. Phys.* 134(2):024105
44. Shu Y, Zhang L, Mai S, Sun S, González L, Truhlar DG. 2020. Implementation of coherent switching with decay of mixing into the SHARC program. *J. Chem. Theory Comput.* 16(6):3464–75
45. Subotnik JE, Ouyang W, Landry BR. 2013. Can we derive Tully's surface-hopping algorithm from the semiclassical quantum Liouville equation? Almost, but only with decoherence. *J. Chem. Phys.* 139(21):214107
46. Wang L, Sifain AE, Prezhdo OV. 2015. Fewest switches surface hopping in Liouville space. *J. Phys. Chem. Lett.* 6(19):3827–33
47. Kapral R. 2016. Surface hopping from the perspective of quantum-classical Liouville dynamics. *Chem. Phys.* 481:77–83
48. Martens CC. 2016. Surface hopping by consensus. *J. Phys. Chem. Lett.* 7(13):2610–15
49. Coronado E. 2020. Molecular magnetism: from chemical design to spin control in molecules, materials and devices. *Nat. Rev. Mater.* 5(2):87–104
50. Giménez-Santamarina S, Cardona-Serra S, Clemente-Juan JM, Gaita-Ariño A, Coronado E. 2020. Exploiting clock transitions for the chemical design of resilient molecular spin qubits. *Chem. Sci.* 11:10718–28
51. Wasielewski MR, Forbes MDE, Frank NL, Kowalski K, Scholes GD, et al. 2020. Exploiting chemistry and molecular systems for quantum information science. *Nat. Rev. Chem.* 4(9):490–504
52. Ullah A, Cerdá J, Baldoví JJ, Varganov SA, Aragó J, Gaita-Ariño A. 2019. In silico molecular engineering of dysprosocenium-based complexes to decouple spin energy levels from molecular vibrations. *J. Phys. Chem. Lett.* 10(24):7678–83
53. Upadhyay S, Dargyte U, Dergachev VD, Prater RP, Varganov SA, et al. 2019. Spin coherence and optical properties of alkali-metal atoms in solid parahydrogen. *Phys. Rev. A* 100(6):063419

54. Upadhyay S, Dargyte U, Prater RP, Dergachev VD, Varganov SA, et al. 2019. Enhanced spin coherence of rubidium atoms in solid parahydrogen. *Phys. Rev. B* 100(2):024106
55. Heller EJ. 1981. Frozen Gaussians: a very simple semiclassical approximation. *J. Chem. Phys.* 75(6):2923–31
56. Martinez TJ, Ben-Nun M, Levine RD. 1996. Multi-electronic-state molecular dynamics: a wave function approach with applications. *J. Phys. Chem.* 100(19):7884–95
57. Ben-Nun M, Martínez TJ. 2002. Ab initio quantum molecular dynamics. In *Advances in Chemical Physics*, ed. I Prigogine, SA Rice, pp. 439–512. New York: John Wiley & Sons
58. Levine BG, Coe JD, Virshup AM, Martínez TJ. 2008. Implementation of *ab initio* multiple spawning in the Molpro quantum chemistry package. *Chem. Phys.* 347(1–3):3–16
59. Yang S, Martínez TJ. 2011. *Ab initio* multiple spawning: first principles dynamics around conical intersections. In *Conical Intersections. Theory, Computation and Experiment*, ed. W Domcke, DR Yarkony, H Köppel, pp. 347–74. Singapore: World Sci. Publ.
60. Mignolet B, Curchod BFE. 2018. A walk through the approximations of *ab initio* multiple spawning. *J. Chem. Phys.* 148(13):134110
61. Ibele LM, Nicolson A, Curchod BFE. 2020. Excited-state dynamics of molecules with classically driven trajectories and Gaussians. *Mol. Phys.* 118(8):e1665199
62. Fedorov DA, Pruitt SR, Keipert K, Gordon MS, Varganov SA. 2016. Ab initio multiple spawning method for intersystem crossing dynamics: spin-forbidden transitions between $^3B_1$ and $^1A_1$ states of GeH_2. *J. Phys. Chem. A* 120(18):2911–19
63. Fedorov DA, Lykhin AO, Varganov SA. 2018. Predicting intersystem crossing rates with AIMS-DFT molecular dynamics. *J. Phys. Chem. A* 122(13):3480–88
64. Curchod BFE, Rauer C, Marquetand P, González L, Martínez TJ. 2016. Communication: GAIMS—Generalized *Ab Initio* Multiple Spawning for both internal conversion and intersystem crossing processes. *J. Chem. Phys.* 144(10):101102
65. Martínez TJ, Levine RD. 1997. Non-adiabatic molecular dynamics: split-operator multiple spawning with applications to photodissociation. *J. Chem. Soc. Faraday Trans.* 93(5):941–47
66. Yang S, Coe JD, Kaduk B, Martínez TJ. 2009. An "optimal" spawning algorithm for adaptive basis set expansion in nonadiabatic dynamics. *J. Chem. Phys.* 130(13):134113
67. Hack MD, Wensmann AM, Truhlar DG, Ben-Nun M, Martínez TJ. 2001. Comparison of full multiple spawning, trajectory surface hopping, and converged quantum mechanics for electronically nonadiabatic dynamics. *J. Chem. Phys.* 115(3):1172–86
68. Curchod BFE, Glover WJ, Martínez TJ. 2020. SSAIMS—stochastic-selection *ab initio* multiple spawning for efficient nonadiabatic molecular dynamics. *J. Phys. Chem. A* 124(30):6133–43
69. Meyer H-D, Manthe U, Cederbaum LS. 1990. The multi-configurational time-dependent Hartree approach. *Chem. Phys. Lett.* 165(1):73–78
70. Manthe U, Meyer H-D, Cederbaum LS. 1992. Wave-packet dynamics within the multiconfiguration Hartree framework: general aspects and application to NOCl. *J. Chem. Phys.* 97(5):3199–213
71. Beck M, Jäckle A, Worth GA, Meyer H-D. 2000. The multiconfiguration time-dependent Hartree (MCTDH) method: a highly efficient algorithm for propagating wavepackets. *Phys. Rep.* 324(1):1–105
72. Meyer H-D. 2012. Studying molecular quantum dynamics with the multiconfiguration time-dependent Hartree method. *WIREs Comput. Mol. Sci.* 2(2):351–74
73. Vendrell O, Meyer H-D. 2011. Multilayer multiconfiguration time-dependent Hartree method: implementation and applications to a Henon-Heiles Hamiltonian and to pyrazine. *J. Chem. Phys.* 134(4):044135
74. Wang H, Thoss M. 2003. Multilayer formulation of the multiconfiguration time-dependent Hartree theory. *J. Chem. Phys.* 119(3):1289–99
75. Manthe U. 2008. A multilayer multiconfigurational time-dependent Hartree approach for quantum dynamics on general potential energy surfaces. *J. Chem. Phys.* 128(16):164116
76. Wang H, Thoss M. 2008. From coherent motion to localization: dynamics of the spin-boson model at zero temperature. *New J. Phys.* 10(11):115005
77. Worth GA, Robb MA, Burghardt I. 2004. A novel algorithm for non-adiabatic direct dynamics using variational Gaussian wavepackets. *Faraday Discuss.* 127:307–23

78. Richings GW, Polyak I, Spinlove KE, Worth GA, Burghardt I, Lasorne B. 2015. Quantum dynamics simulations using Gaussian wavepackets: the vMCG method. *Int. Rev. Phys. Chem.* 34(2):269–308
79. Lasorne B, Robb MA, Worth GA. 2007. Direct quantum dynamics using variational multi-configuration Gaussian wavepackets. Implementation details and test case. *Phys. Chem. Chem. Phys.* 9(25):3210–27
80. Burghardt I, Meyer H-D, Cederbaum LS. 1999. Approaches to the approximate treatment of complex molecular systems by the multiconfiguration time-dependent Hartree method. *J. Chem. Phys.* 111(7):2927–39
81. Worth GA, Meyer H-D, Köppel H, Cederbaum LS, Burghardt I. 2008. Using the MCTDH wavepacket propagation method to describe multimode non-adiabatic dynamics. *Int. Rev. Phys. Chem.* 27(3):569–606
82. Mukherjee B, Naskar K, Mukherjee S, Ghosh S, Sahoo T, Adhikari S. 2019. Beyond Born-Oppenheimer theory for spectroscopic and scattering processes. *Int. Rev. Phys. Chem.* 38(3–4):287–341
83. Naskar K, Mukherjee S, Mukherjee B, Ravi S, Mukherjee S, et al. 2020. ADT: a generalized algorithm and program for beyond Born-Oppenheimer equations of "*N*" dimensional sub-Hilbert space. *J. Chem. Theory Comput.* 16(3):1666–80
84. Baer M. 2006. *Beyond Born-Oppenheimer: Conical Intersections and Electronic Nonadiabatic Coupling Terms*. Hoboken, NJ: John Wiley & Sons
85. Köppel H, Domcke W, Cederbaum LS. 2007. Multimode molecular dynamics beyond the Born-Oppenheimer approximation. In *Advances in Chemical Physics*, Vol. 57, ed. I Prigogine, S Rice, pp. 59–246. Hoboken, NJ: John Wiley & Sons
86. Lévêque C, Taïeb R, Köppel H. 2014. Communication: Theoretical prediction of the importance of the $^3B_2$ state in the dynamics of sulfur dioxide. *J. Chem. Phys.* 140(9):091101
87. Penfold TJ, Spesyvtsev R, Kirkby OM, Minns RS, Parker DSN, et al. 2012. Quantum dynamics study of the competing ultrafast intersystem crossing and internal conversion in the "channel 3" region of benzene. *J. Chem. Phys.* 137(20):204310
88. Capano G, Chergui M, Rothlisberger U, Tavernelli I, Penfold TJ. 2014. A quantum dynamics study of the ultrafast relaxation in a prototypical Cu(I)-phenanthroline. *J. Phys. Chem. A* 118(42):9861–69
89. Eng J, Gourlaouen C, Gindensperger E, Daniel C. 2015. Spin-vibronic quantum dynamics for ultrafast excited-state processes. *Acc. Chem. Res.* 48(3):809–17
90. Falahati K, Tamura H, Burghardt I, Huix-Rotllant M. 2018. Ultrafast carbon monoxide photolysis and heme spin-crossover in myoglobin via nonadiabatic quantum dynamics. *Nat. Commun.* 9:4502
91. Domcke W, Mishra S, Poluyanov LV. 2006. The relativistic $E \times E$ Jahn-Teller effect revisited. *Chem. Phys.* 322(3):405–10
92. Poluyanov LV, Domcke W. 2008. The $^3E \times E$, $^4E \times E$ and $^5E \times E$ Jahn-Teller Hamiltonians of trigonal systems. *Chem. Phys.* 352(1–3):125–34
93. Mondal P, Opalka D, Poluyanov LV, Domcke W. 2011. Jahn-Teller and spin-orbit coupling effects in transition-metal trifluorides. *Chem. Phys.* 387(1–3):56–65
94. Weike T, Eisfeld W. 2016. Development of multi-mode diabatic spin-orbit models at arbitrary order. *J. Chem. Phys.* 144(10):104108
95. Poluyanov LV, Domcke W, Mishra S. 2019. Spin-orbit vibronic coupling in $^4\Pi$ states of linear triatomic molecules. *J. Chem. Phys.* 151(13):134103
96. Lischka H, Nachtigallová D, Aquino AJA, Szalay PG, Plasser F, et al. 2018. Multireference approaches for excited states of molecules. *Chem. Rev.* 118(15):7293–361
97. Mai S, Atkins AJ, Plasser F, González L. 2019. The influence of the electronic structure method on intersystem crossing dynamics. The case of thioformaldehyde. *J. Chem. Theory Comput.* 15(6):3470–80
98. Conte R, Qu C, Houston PL, Bowman JM. 2020. Efficient generation of permutationally invariant potential energy surfaces for large molecules. *J. Chem. Theory Comput.* 16(5):3264–72
99. Zhu X, Yarkony DR. 2014. Fitting coupled potential energy surfaces for large systems: method and construction of a 3-state representation for phenol photodissociation in the full 33 internal degrees of freedom using multireference configuration interaction determined data. *J. Chem. Phys.* 140(2):024112
100. Shen Y, Yarkony DR. 2020. Construction of quasi-diabatic Hamiltonians that accurately represent *ab initio* determined adiabatic electronic states coupled by conical intersections for systems on the order of 15 atoms. Application to cyclopentoxide photoelectron detachment in the full 39 degrees of freedom. *J. Phys. Chem. A* 124(22):4539–48

101. Casanova D, Krylov AI. 2020. Spin-flip methods in quantum chemistry. *Phys. Chem. Chem. Phys.* 22(8):4326–42
102. Schmidt MW, Gordon MS. 1998. The construction and interpretation of MCSCF wavefunctions. *Annu. Rev. Phys. Chem.* 49:233–66
103. Frutos LM, Andruniow T, Santoro F, Ferre N, Olivucci M. 2007. Tracking the excited-state time evolution of the visual pigment with multiconfigurational quantum chemistry. *PNAS* 104(19):7764–69
104. Snyder JW, Parrish RM, Martínez TJ. 2017. α-CASSCF: an efficient, empirical correction for SA-CASSCF to closely approximate MS-CASPT2 potential energy surfaces. *J. Phys. Chem. Lett.* 8(11):2432–37
105. Granucci G, Toniolo A. 2000. Molecular gradients for semiempirical CI wavefunctions with floating occupation molecular orbitals. *Chem. Phys. Lett.* 325(1–3):79–85
106. Hollas D, Šištík L, Hohenstein EG, Martínez TJ, Slavíček P. 2018. Nonadiabatic ab initio molecular dynamics with the floating occupation molecular orbital-complete active space configuration interaction method. *J. Chem. Theory Comput.* 14(1):339–50
107. Peng W-T, Levine BG. 2019. Ab initio molecular dynamics study of the interaction between defects during nonradiative recombination. *J. Phys. Chem. C* 123(27):16588–95
108. Marian CM. 2012. Spin-orbit coupling and intersystem crossing in molecules. *WIREs Comput. Mol. Sci.* 2(2):187–203
109. Nakajima T, Hirao K. 2012. The Douglas-Kroll-Hess approach. *Chem. Rev.* 112(1):385–402
110. Roos BO, Malmqvist P. 2004. Relativistic quantum chemistry: the multiconfigurational approach. *Phys. Chem. Chem. Phys.* 6(11):2919–27
111. Berning A, Schweizer M, Werner H-J, Knowles PJ, Palmieri P. 2000. Spin-orbit matrix elements for internally contracted multireference configuration interaction wavefunctions. *Mol. Phys.* 98(21):1823–33
112. Franco de Carvalho F, Curchod BFE, Penfold TJ, Tavernelli I. 2014. Derivation of spin-orbit couplings in collinear linear-response TDDFT: a rigorous formulation. *J. Chem. Phys.* 140(14):144103
113. Chiodo SG, Leopoldini M. 2014. MolSOC: a spin–orbit coupling code. *Comput. Phys. Commun.* 185(2):676–83
114. Li Z, Suo B, Zhang Y, Xiao Y, Liu W. 2013. Combining spin-adapted open-shell TD-DFT with spin-orbit coupling. *Mol. Phys.* 111(24):3741–55
115. Neese F. 2005. Efficient and accurate approximations to the molecular spin-orbit coupling operator and their use in molecular *g*-tensor calculations. *J. Chem. Phys.* 122(3):034107
116. Pokhilko P, Epifanovsky E, Krylov AI. 2019. General framework for calculating spin-orbit couplings using spinless one-particle density matrices: theory and application to the equation-of-motion coupled-cluster wave functions. *J. Chem. Phys.* 151(3):034106
117. Forde A, Inerbaev T, Kilin D. 2018. Spinor dynamics in pristine and Mn^{2+}-doped $CsPbBr_3$ NC: role of spin-orbit coupling in ground- and excited-state dynamics. *J. Phys. Chem. C* 122(45):26196–213
118. Valentine AJS, Li X. 2019. Toward the evaluation of intersystem crossing rates with variational relativistic methods. *J. Chem. Phys.* 151(8):084107
119. Rosaleny LE, Zinovjev K, Tuñón I, Gaita-Ariño A. 2019. A first peek into sub-picosecond dynamics of spin energy levels in magnetic biomolecules. *Phys. Chem. Chem. Phys.* 21(21):10908–13
120. Bellonzi N, Medders GR, Epifanovsky E, Subotnik JE. 2019. Configuration interaction singles with spin-orbit coupling: constructing spin-adiabatic states and their analytical nuclear gradients. *J. Chem. Phys.* 150(1):014106
121. Bellonzi N, Alguire E, Fatehi S, Shao Y, Subotnik JE. 2020. TD-DFT spin-adiabats with analytic nonadiabatic derivative couplings. *J. Chem. Phys.* 152(4):044112
122. Xie C, Hu X, Zhou L, Xie D, Guo H. 2013. *Ab initio* determination of potential energy surfaces for the first two UV absorption bands of SO_2. *J. Chem. Phys.* 139:014305
123. Mai S, Marquetand P, González L. 2014. Non-adiabatic and intersystem crossing dynamics in SO_2. II. The role of triplet states in the bound state dynamics studied by surface-hopping simulations. *J. Chem. Phys.* 140(20):204302
124. Franco de Carvalho F, Tavernelli I. 2015. Nonadiabatic dynamics with intersystem crossings: a time-dependent density functional theory implementation. *J. Chem. Phys.* 143(22):224105

125. Plasser F, Gómez S, Menger MFSJ, Mai S, González L. 2019. Highly efficient surface hopping dynamics using a linear vibronic coupling model. *Phys. Chem. Chem. Phys.* 21(1):57–69
126. Barca GMJ, Bertoni C, Carrington L, Datta D, De Silva N, et al. 2020. Recent developments in the general atomic and molecular electronic structure system. *J. Chem. Phys.* 152(15):154102
127. Fedorov DG, Gordon MS. 2000. A study of the relative importance of one and two-electron contributions to spin-orbit coupling. *J. Chem. Phys.* 112(13):5611–23
128. Snyder JW, Curchod BFE, Martínez TJ. 2016. GPU-accelerated state-averaged complete active space self-consistent field interfaced with ab initio multiple spawning unravels the photodynamics of provitamin D_3. *J. Phys. Chem. Lett.* 7(13):2444–49
129. Mai S, Marquetand P, Richter M, González-Vázquez J, González L. 2013. Singlet and triplet excited-state dynamics study of the keto and enol tautomers of cytosine. *Chem. Phys. Chem.* 14(13):2920–31
130. Richter M, Mai S, Marquetand P, González L. 2014. Ultrafast intersystem crossing dynamics in uracil unravelled by *ab initio* molecular dynamics. *Phys. Chem. Chem. Phys.* 16(44):24423–36
131. Crespo-Hernández CE, Martínez-Fernández L, Rauer C, Reichardt C, Mai S, et al. 2015. Electronic and structural elements that regulate the excited-state dynamics in purine nucleobase derivatives. *J. Am. Chem. Soc.* 137(13):4368–81
132. Marazzi M, Mai S, Roca-Sanjuán D, Delcey MG, Lindh R, et al. 2016. Benzophenone ultrafast triplet population: revisiting the kinetic model by surface-hopping dynamics. *J. Phys. Chem. Lett.* 7(4):622–26
133. Atkins AJ, González L. 2017. Trajectory surface-hopping dynamics including intersystem crossing in $[Ru(bpy)_3]^{2+}$. *J. Phys. Chem. Lett.* 8(16):3840–45
134. Mai S, Richter M, Marquetand P, González L. 2017. The DNA nucleobase thymine in motion—intersystem crossing simulated with surface hopping. *Chem. Phys.* 482:9–15
135. Mai S, Pollum M, Martínez-Fernández L, Dunn N, Marquetand P, et al. 2016. The origin of efficient triplet state population in sulfur-substituted nucleobases. *Nat. Commun.* 7:13077
136. Hoffmann MR, Schatz GC. 2000. Theoretical studies of intersystem crossing effects in the $O+H_2$ reaction. *J. Chem. Phys.* 113(21):9456–65
137. Maiti B, Schatz GC, Lendvay G. 2004. Importance of intersystem crossing in the $S(^3P, ^1D) + H_2 \rightarrow SH + H$ reaction. *J. Phys. Chem. A* 108(41):8772–81
138. Czakó G, Shepler BC, Braams BJ, Bowman JM. 2009. Accurate *ab initio* potential energy surface, dynamics, and thermochemistry of the $F + CH_4 \rightarrow HF + CH_3$ reaction. *J. Chem. Phys.* 130(8):084301
139. Fu B, Shepler BC, Bowman JM. 2011. Three-state trajectory surface hopping studies of the photodissociation dynamics of formaldehyde on ab initio potential energy surfaces. *J. Am. Chem. Soc.* 133(20):7957–68
140. Fu B, Han YC, Bowman JM, Angelucci L, Balucani N, et al. 2012. Intersystem crossing and dynamics in $O(^3P) + C_2H_4$ multichannel reaction: experiment validates theory. *PNAS* 109(25):9733–38
141. Balucani N, Leonori F, Casavecchia P, Fu B, Bowman JM. 2015. Crossed molecular beams and quasiclassical trajectory surface hopping studies of the multichannel nonadiabatic $O(^3P)$ + ethylene reaction at high collision energy. *J. Phys. Chem. A* 119(50):12498–511
142. Fumanal M, Gindensperger E, Daniel C. 2017. Ultrafast excited-state decays in $[Re(CO)_3(N,N)(L)]^{n+}$: nonadiabatic quantum dynamics. *J. Chem. Theory Comput.* 13(3):1293–306
143. Alexander MH, Capecchi G, Werner H-J. 2002. Theoretical study of the validity of the Born-Oppenheimer approximation in the $Cl + H_2 \rightarrow HCl + H$ reaction. *Science* 296(5568):715–18
144. Althorpe SC, Clary DC. 2003. Quantum scattering calculations on chemical reactions. *Annu. Rev. Phys. Chem.* 54:493–529
145. Marthe U, Capecchi G, Werner HJ. 2004. The effect of spin-orbit coupling on the thermal rate constant of the $H_2 + Cl \rightarrow H + HCl$ reaction. *Phys. Chem. Chem. Phys.* 6(21):5026–30
146. Che L, Ren Z, Wang X, Dong W, Dai D, et al. 2007. Breakdown of the Born-Oppenheimer approximation in the $F + o\text{-}D_2 \rightarrow DF + D$ reaction. *Science* 317(5841):1061–64
147. Alexander MH, Manolopoulos DE, Werner H-J. 2000. An investigation of the $F+H_2$ reaction based on a full *ab initio* description of the open-shell character of the $F(^2P)$ atom. *J. Chem. Phys.* 113(24):11084–100
148. Li G, Werner H-J, Lique F, Alexander MH. 2007. New *ab initio* potential energy surfaces for the $F + H_2$ reaction. *J. Chem. Phys.* 127(17):174302

149. Chen J, Sun Z, Zhang DH. 2015. An accurate potential energy surface for the F + H_2 → HF + H reaction by the coupled-cluster method. *J. Chem. Phys.* 142(2):024303
150. Tzeng Y-R, Alexander MH. 2004. Role of the F spin-orbit excited state in the F+HD reaction: contributions to the dynamical resonance. *J. Chem. Phys.* 121(11):5183–90
151. Zhang Y, Xie T-X, Han K-L, Zhang JZH. 2004. The investigation of spin-orbit effect for the F(^{2}P) + HD reaction. *J. Chem. Phys.* 120(13):6000–4
152. Lique F, Alexander MH, Li G, Werner H-J, Nizkorodov SA, et al. 2008. Evidence for excited spin-orbit state reaction dynamics in F + H_2: theory and experiment. *J. Chem. Phys.* 128(8):084313
153. Tscherbul TV, Kłos J. 2020. Magnetic tuning of ultracold barrierless chemical reactions. *Phys. Rev. Res.* 2(1):013117

Annual Review of
Physical Chemistry
Volume 72, 2021

Contents

Errata

An online log of corrections to *Annual Review of Physical Chemistry* articles may be found at http://www.annualreviews.org/errata/physchem